Master's thesis

# Process-based modelling of bank-breaking mechanisms of tidal sandbanks

*Author:*
Thomas J. Van Veelen

*Graduation committee:*
Dr. Ir. Pieter C. Roos
Prof. Dr. Suzanne J.M.H. Hulscher

November 11, 2016

UNIVERSITY OF TWENTE.

# Preface

This thesis may look slightly different than others, because it is written in the form of a paper, which is to be published in a peer-reviewed scientific journal. This means that the writing is to the the point and emphasis is put on results and discussion. The underlying mathematics and model data are included to an extent with which the results can be reproduced, but those who would like more thorough information (e.g. additional equations, mathematical techniques, model data or runs and figures on which the sensitivity analysis is based) are always welcome to contact me. Space has not always been my best friend.

That being said, I am proud on the presented thesis. It is the result of six months of sweat, thoughts, tears and lots of errors along the way. Luckily, there were many people to support me during the whole process and without whom I would not have been to finish this work. First of all, I would like to thank Pieter, my daily supervisor, who was available at any moment to answer questions, provide new ideas and lots of justified feedback on the thesis and on soccer with his motivating enthusiasm. Next, I would like to thank Suzanne, the head of my graduation committee, who gave me the confidence and freedom to explore my own ideas, while also keeping me on the path to graduation with practical feedback and support in important decisions. I would also like to thank my parents for their support during the times I have been struggling with the thesis and many other things and Wouter for the distractions in the form of movies. Also, a big thanks to all the people with whom I shared the office, Wietse, Mick, Luuk, Sven, Larisse and Chris, for all walks and talks and the pleasant working atmosphere. And last but not least, all my friends who made life in (and outside) Enschede enjoyable, thanks to all of you.

*Thomas van Veelen*
*November, 2016*

**Ocean Dynamics manuscript No.**
(will be inserted by the editor)

# Process-based modelling of bank-breaking mechanisms of tidal sandbanks

**Thomas J. van Veelen · Pieter C. Roos · Suzanne J. M. H. Hulscher**

Received: date / Accepted: date

**Abstract** To improve our understanding of transient long-term plan view dynamics of tidal sandbanks, we have developed a nonlinear idealized morphodynamic model. Current mechanisms describe how an isolated bank breaks into multiple banks, but they lack process-based support. We aim to provide such support with the inclusion of nonlinear interactions between tidal flow, topography, Coriolis and bottom friction in the hydrodynamic formulation and depth-dependent wind wave stirring and slope effects in the bedload sediment transport formulation.

We distinguish three generic evolution paths. (I) Rotation of the bank ends towards the preferred angle of deposition and separate growth, causing bank-breaking. (II) Rotation of the bank ends towards the preferred angle of deposition and central growth, triggering an S-shape. (III) Straight outline and central growth, triggering an S-shape, but much faster than path II. In addition to the path-dependent dynamics, the banks also experience pattern expansion, elongation and amplitude growth.

Bank-breaking (path I) requires two condition. The initial bank may not have an orientation in the angle of preferred deposition and must be sufficiently long to trigger separate growth. Alternatively, the nonlinear flow response to an elevated centre triggers evolution towards an S-shape. The proposed paths are consistent with mechanisms in Huthnance (1982b) and Smith (1988). The characteristic final S-shape shows resemblance to meandering banks in the North Sea.

T. J. van Veelen
University of Twente
E-mail: t.j.vanveelen@student.utwente.nl

P. C. Roos
University of Twente

S. J. M. H. Hulscher
University of Twente

**Keywords** Tidal sandbanks · Bank-breaking mechanisms · Non-linear morphodynamics · Proces-based modelling

## 1 Introduction

Offshore tidal sandbanks occur in patches throughout shallow shelf seas, such as the North Sea. With lengths in the order of tens of kilometres, widths of five to ten kilometres and heights of tens of metres, they are the largest in the class of tide-driven rhythmic bottom features (Dyer and Huntley 1999). Additionally, sandbanks generally have an orientation of 0 to 20 degrees anticlockwise with respect to the principal tidal current on the Northern Hemisphere (Kenyon et al 1981) and migrate with a speed of around 1 m/year (Knaapen 2005). Their slow evolution, typically on a time scale of centuries, makes it unclear whether they are in equilibrium (Dyer and Huntley 1999).

Understanding the dynamics of tidal sandbanks is of both scientific and practical interest. They provide an attractive option for the extraction of aggregates (Van Lancker et al 2010), a habitat for marine flora an fauna (Kaiser et al 2004; Atalah et al 2012), a foundation for wind farms (Whitehouse et al 2011; Fairley et al 2016) and those closer to the coast serve as coastal protection (Dolphin et al 2007). This wide range of interests emphasizes the relevance to understand the natural dynamics as well as the response to human interventions. This paper focusses on the former, i.e. the inherent behaviour.

To gain insight into the bank-building mechanisms, many banks have been investigated. For example, Caston and Stride (1970) used sandwave observations to derive residual circulating currents around the Norfolk banks, indicating a link between currents and topography. The interactions between tides and topography were investigated by Huthnance (1982a,b), De Vriend (1990) and Hulscher et al (1993), who explained

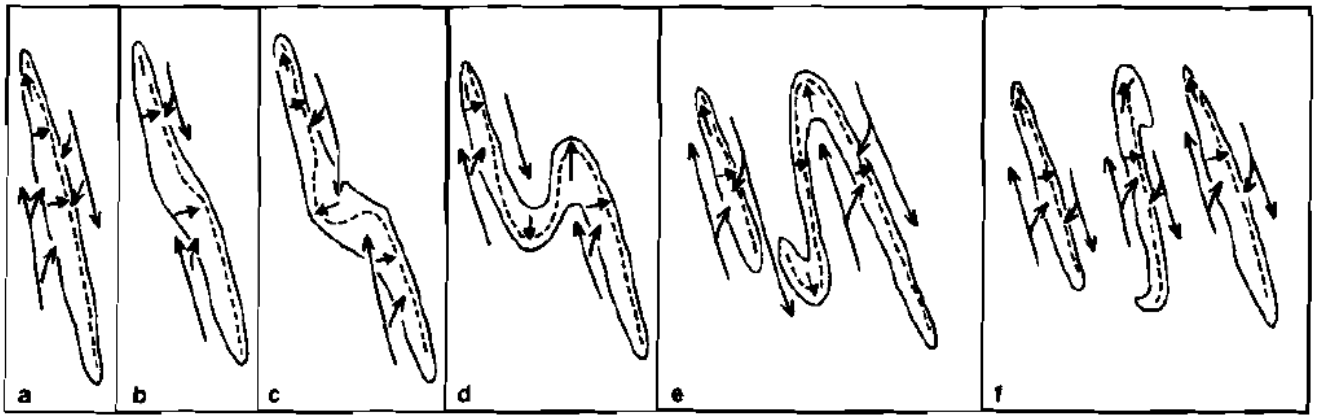


**Fig. 1** Breaking mechanism as proposed by Caston (1972): (a) Linear sand body parallel to the direction of the tidal currents, (b) slight "kink" present, possibly due to unequal rate of transport, (c) evolution towards a double curve, (d) the double curve becomes an incipient pair of ebb and flood channels, (e) the channels lengthen, resulting in "blow outs" in the bank, (f) the bank breaks into three parts. The arrows represent the principal tidal flow lines.

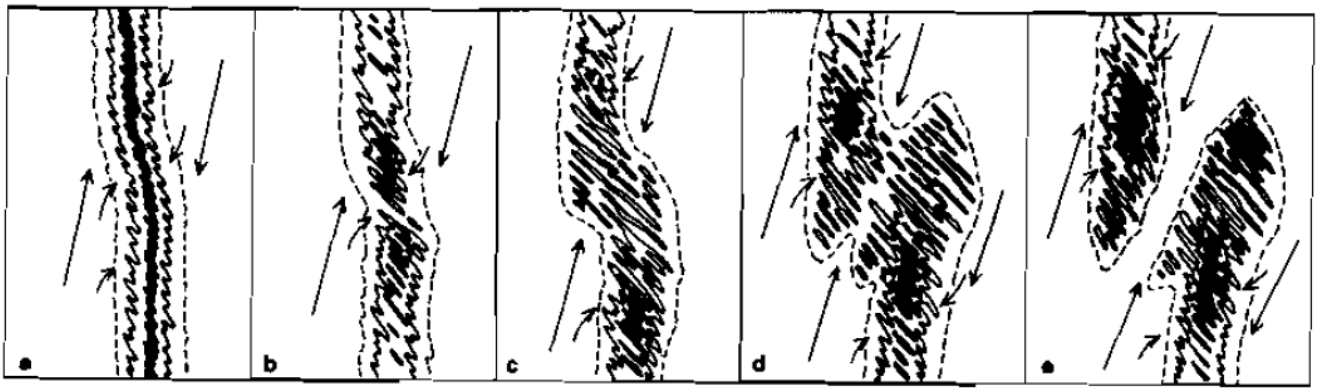


**Fig. 2** Breaking mechanism proposed by Smith (1988): (a) asymmetric sandbank, which is aligned slightly oblique to the tidal currents, has a small kink and sandwaves on top, (b) the sand carried in from both sides of the banks is incorporated in the sand waves at both sides of the kink, which results in a topographic low at the kink, (c) the topographic low becomes a trough, (d) the sand wave fields at both ends drift apart apart, resulting in a passageway, and (e) a characteristic head and tail, when the banks have broken. The arrows represent the principal tidal flow lines.

sandbanks as free instabilities of a sandy seabed subject to tidal flow. Roos et al (2008) showed how the formation process can be triggered by a local topographic disturbance, such as a sand extraction pit. This was all done with linear analyses of idealised process-based models. These are however restricted to the initial stage of bank formation.

Idealised models have been extended to finite-amplitude behaviour by Huthnance (1982a) and Roos et al (2004). Both obtained equilibrium profiles for tidal sandbanks, but under the restriction of parallel depth contours. In an extended version of his linear stability model, Huthnance (1982b) dropped this restriction and managed to find two-dimensional equilibrium profiles. However, he used simplified flow conditions (block flow, omitting inertial terms and negligence of Coriolis force) and restrictive sediment availability.

Via a complex numerical hydrodynamic model, Sanay et al (2007) reproduced flow circulations around the Norfolk bank. Similar results were obtained at many other North Sea locations, e.g. Middelkerke Banks (Williams et al 2000; Pan et al 2007), Hinder Banks (Deleu et al 2004), Great Yarmouth Banks (Horrillo-Caraballo and Reeve 2008) and Kwinte Bank (Brière et al 2010; Van den Eynde et al 2010). Coupled with a morphodynamic module, the numerical models showed how the resulting sediment transport contributes to the stability of the banks. However, it proved to be hard to identify the processes relevant on the time scale of centuries on which sandbanks evolve.

Due to the restrictions of both idealised and complex numerical modelling, research into long-term plan view morphodynamics is limited to two descriptive hypotheses and one model result. Caston (1972) suggested that an isolated bank will break into three separate banks, based on his observations of the Norfolk banks (Fig. 1). Smith (1988) proposed a different breaking mechanism, based on his observations of the Hinder banks, where an isolated bank breaks into two separate banks (Fig. 2). This mechanism is supported by analysis from Deleu et al (2004). However, both hypotheses yet lack process-based support.

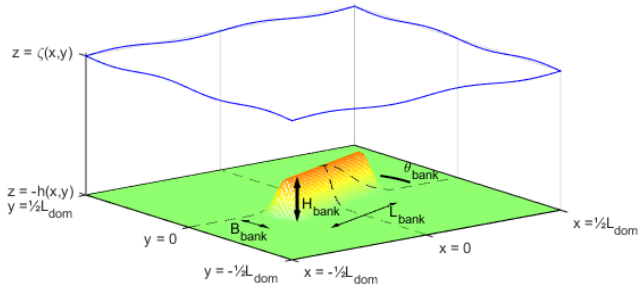


**Fig. 3** Schematization of the formulated domain. It is square with length $L_{dom}$ and periodic boundaries. A sandbank is put on an otherwise flat bed. Its initial topography $h(x,y)$ is characterized by bank length $L_{bank}$, bank width $B_{bank}$, bank height $h_{bank}$ and the angle between the the major bank axis and principal tidal flow (here along the $x$-axis) $\theta_{bank}$. Finally, $\zeta(x,y)$ denotes the surface water level.

In his aforementioned extended linear stability model, Huthnance (1982b) aimed to provide such process-based support. He observes bank elongation, evolution towards an S-shape and rotation towards the angle of preferred deposition in the finite-amplitude regime. Although many interesting bank patterns are shown, a systematic analysis of the driving physics is absent and the simplifications should be kept in mind.

The present study aims to provide systematic process-based support for long-term morphological behaviour of tidal sandbanks. To this end, we develop an idealised model, which includes the essential processes, nonlinear dynamics and a topography that varies in both horizontal directions. This model will be used to study the long-term behaviour of isolated sandbanks subject to tidal flow. We focus on transient behaviour, such as the conditions for bank-breaking to occur, and do not aim to obtain equilibrium bank configurations. Furthermore, we will systematically vary the initial topography of the bank to investigate its effect on the long-term evolution.

The outline of this paper is as follows: first, the model formulation is introduced in section 2. Next, the solution procedure is presented in section 3, followed by the results in section 4 and the discussion in section 5. Finally, conclusions are drawn in section 6.

## 2 Model formulation

### 2.1 Geometry

Consider an offshore region of a shallow shelf sea, far away from coastal boundaries. Here, influences of a coastline and shelf slope are neglected. The mean water depth $H^*$ is in the order of 20 - 30 m, with an asterisk denoting an unscaled variable. The model consists of a squared domain with spatially periodic boundaries (Fig. 3). On the domain, tidal sandbanks are described by a spatiotemporally varying bed level $z^* = -h^*(x^*, y^*, t^*)$.

### 2.2 Model equations

The model is kept as simple as possible, while still retaining the essential physics. In line with earlier studies, we adopt depth-averaged flow (e.g. Huthnance 1982a,b; Hulscher et al 1993; Roos et al 2008). Tidal flow velocity $(u^*, v^*)$ is characterized by a dominating semidiurnal lunar component ($M_2$ with angular frequency $\sigma^* = 1.405 \times 10^{-4}$ rad/s) with a maximum flow velocity $U^*$, typically $0.5 - 1.0$ m/s. Furthermore, bed friction and the Coriolis effect are included to capture the mechanism of tidal rectification (e.g. Pattiaratchi and Collins 1987). Conservation of momentum and mass is expressed by the nonlinear depth-averaged shallow water equations, which take the following form:

$$\frac{\partial u^*}{\partial t^*} + u^*\frac{\partial u^*}{\partial x^*} + v^*\frac{\partial u^*}{\partial y^*} - f^*v^* + \frac{r^*u^*}{h^*+\zeta^*} = -F^* - g^*\frac{\partial \zeta^*}{\partial x^*}, \quad (1)$$

$$\frac{\partial v^*}{\partial t^*} + u^*\frac{\partial v^*}{\partial x^*} + v^*\frac{\partial v^*}{\partial y^*} + f^*u^* + \frac{r^*v^*}{h^*+\zeta^*} = -G^* - g^*\frac{\partial \zeta^*}{\partial y^*}, \quad (2)$$

$$\frac{\partial h^*+\zeta^*}{\partial t^*} + \frac{\partial (h^*+\zeta^*)u^*}{\partial x^*} + \frac{\partial (h^*+\zeta^*)v^*}{\partial y^*} = 0. \quad (3)$$

Here, $f^* = 2\Omega^*\sin\varphi$ denotes the Coriolis parameter (with the angular frequency of the Earth's rotation $\Omega^* = 7.292 \times 10^{-5}$ rad/s and latitude $\varphi$). Following Lorentz' linearisation, $r^* = \frac{8}{3\pi}c_d U^*$ denotes the linear friction coefficient (with dimensionless drag coefficient $c_d$). This is widely employed in model studies of large-scale seabed dynamics to retain the by the flow experienced bottom friction over a tidal cycle (e.g. Zimmerman 1982; Huthnance 1982a,b; Roos and Hulscher 2003). Furthermore, $g^* = 9.81$ m/s$^2$ is the gravitational acceleration and $(F^*, G^*)$ are spatially uniform yet time-dependent forcing terms. They will be specified in section 2.4.

Considering sediment transport, the model is restricted to bed load transport only. This mode drives bank growth and has been proven to establish equilibria in a model environment (Roos and Hulscher 2004). The essential properties to be included are: 1. a higher order (larger than 1) power dependency of sediment transport on flow velocity; 2. a bed slope effect; 3. depth-dependent sediment stirring by wind waves. Following earlier studies (e.g. Hulscher et al 1993), a third order power law is adopted. Additionally, wind wave velocities $(u_w^*, v_w^*)$ with an amplitude $U_w = 0.6$ m/s drive sediment stirring. They do not have a preferred direction and storms are excluded. These properties result in the following (wind wave-averaged) sediment transport formula:

$$\vec{q}^* = \alpha^*\left(|\vec{u}^*|^2 + \frac{1}{2}U_w^{*2}\left[\frac{h^*}{H^*}\right]^{-\kappa}\right)(\vec{u}^* + \lambda^*\vec{\nabla}^* h^*). \quad (4)$$

Here, $\vec{q}^* = (q_x^*, q_y^*)$ is the sediment transport flux in m$^2$/s, $\alpha^*$ is a proportionality coefficient in s$^2$/m (Van Rijn 1993) and $\kappa = 2$ is a power to control the depth effects of wind wave stirring. Furthermore, $\lambda^* = \tilde{\lambda}^* U^*$ is a bed slope coefficient in m/s, which describes the preferred downhill movement of the sediment (with $\tilde{\lambda}$ inversely proportional to the angle of repose (Sekine and Parker 1992)). Moreover, $\vec{\nabla}^* = (\partial/\partial x^*, \partial/\partial y^*)$ is the (dimensional) horizontal nabla operator.

Finally, bed evolution is computed using the commonly employed Exner's equation, in which the bed evolution is a function of the divergence of the sediment fluxes:

$$(1-\varepsilon_{por})\frac{\partial h^*}{\partial t^*} = \vec{\nabla}^* \cdot \vec{q}^* \,. \tag{5}$$

Herein, $\varepsilon_{por} = 0.4$ denotes the porosity of the seabed (typically 0.4).

## 2.3 Scaling

We introduce dimensionless coordinates (without asterisk) according to

$$(x,y) = \tfrac{(x^*,y^*)}{L^*}\,, \quad z = \tfrac{z^*}{H^*}\,, \quad t = \sigma^* t^*\,, \quad t_{mor} = \tfrac{t^*}{T^*_{mor}}\,.$$

Herein, the tidal excursion length $L^* = U^*/\sigma^*$ serves as the horizontal length scale and the mean water depth $H^*$ serves as the vertical length scale. Two time scales are introduced to distinguish between short-term (tidal cycle) and long-term (scale of bed evolution) dynamics: a tidal time coordinate $t$ for the hydrodynamics and sediment fluxes, and a slower morphological time coordinate $t_{mor}$ for bed evolution, with $T_{mor} = (1-\varepsilon_{por})\frac{H^* L^*}{\alpha^* U^{*\beta}}$. This means that the bed level is a function of $t_{mor}$ but not of $t$. Note that equation (4) was already averaged over the shorter time scale of wind waves.

Next, we introduce scaled quantities according to

$$(u,v) = \tfrac{(u^*,v^*)}{U^*}\,, \quad h = \tfrac{h^*}{H^*}\,, \quad \zeta = \tfrac{g^*\zeta^*}{U^{*2}}\,, \quad (q_x,q_y) = \tfrac{(q_x^*,q_y^*)}{\alpha^* U^{*\beta}}\,.$$

In terms of the scaled coordinates and quantities, the hydrodynamic model equations (1)-(3) become:

$$\frac{\partial u}{\partial t} + u\frac{\partial u}{\partial x} + v\frac{\partial u}{\partial y} - fv + \frac{ru}{h} = -F - \frac{\partial \zeta}{\partial x}\,, \tag{6}$$

$$\frac{\partial v}{\partial t} + u\frac{\partial v}{\partial x} + v\frac{\partial v}{\partial y} + fu + \frac{rv}{h} = -G - \frac{\partial \zeta}{\partial y}\,, \tag{7}$$

$$\frac{\partial (hu)}{\partial x} + \frac{\partial (hv)}{\partial y} = 0\,. \tag{8}$$

Herein, we have introduced scaled Coriolis and friction coefficients, $f = \frac{f^*}{\sigma^*}$ respectively $r = \frac{r^*}{\sigma^* H^*}$, and $(F,G) = \frac{(F^*,G^*)}{U^*\sigma^*}$ represents the dimensionless forcing. Furthermore, we apply the rigid lid assumption. This means that the contribution of the free surface elevation to the mean water depth is neglected, which is justified, because the squared Froude Number $Fr^2 = \frac{U^{*2}}{g^* H^*} \approx 2\times 10^{-3}$ is negligible. It is also found that the bed level change $\frac{\partial h}{\partial t_{mor}}$ is negligible in the continuity equation for tidal flow (Eq. 8), because $1/(\sigma^* T^*_{mor}) \approx 10^{-6}$. Hence, the hydrodynamic calculations can be decoupled from the sediment transport and the bed evolution, which is commonly known as the quasi-stationary approach.

Next, the scaled equation for sediment transport becomes:

$$\vec{q} = \left(|\vec{u}|^2 + \frac{1}{2}U_w^2 h^{-\kappa}\right)(\vec{u} + \lambda \vec{\nabla} h)\,. \tag{9}$$

Herein, $U_w = \frac{U^*_w}{U^*}$ and $\lambda = \frac{\lambda^* H^*}{L^* U^*}$. Finally, the scaled version of Exner's equation, i.e. Eq. (5) becomes:

$$\frac{\partial h}{\partial t_{mor}} = \vec{\nabla} \cdot \langle \vec{q} \rangle\,. \tag{10}$$

The brackets denote averaging over a tidal cycle: $\langle \cdot \rangle = \frac{1}{2\pi}\int_0^{2\pi} \cdot\, dt$. Because of the quasi-stationary approach, only the tidally averaged sediment flux effectively contributes to the bed evolution.

## 2.4 Tidal forcing

The tidal forcing represents a spatially uniform yet time-dependent pressure gradient, which is written as a truncated Fourier series:

$$(F,G) = \sum_{p=-2}^{2} (F_p, G_p)\exp(ip\sigma t)\,. \tag{11}$$

Herein, $p = 0$ denotes the residual component of the tidal flow, $p = \pm 1$ denotes the components of an $M_2$-tide and $p = \pm 2$ denotes the components of the first overtide ($M_4$). $(F_p, G_p)$ are complex Fourier coefficients which relate to the Fourier coefficients of tidal flow over a flat bed $(U_{0p}, V_{0p})$, i.e. excluding the interaction with topography:

$$F_p = -(ip + \frac{r}{h_0})U_{0p} + fV_{0p}\,, \tag{12}$$

$$G_p = -(ip + \frac{r}{h_0})V_{0p} - fU_{0p}\,. \tag{13}$$

We have specified the tidal forcing terms such that they fulfil equations (1) and (2). The complex Fourier coefficients $(U_{0p}, V_{0p})$ include the magnitude $\gamma_0$ and direction $\vartheta_0$ in case of the residual flow ($p = 0$) or semi-major axis $\gamma_p$, ellipticy $\varepsilon_p$, inclination $\vartheta_p$ and phase $\psi_p$ for an $M_2$- or $M_4$-tide. The relations can be found in appendix A.

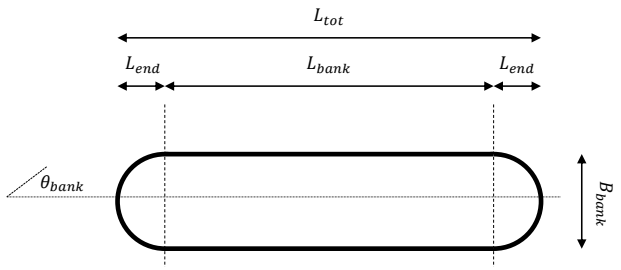


**Fig. 4** Top view of the initial sandbank topography. We distinguish a main part, with length $L_{bank}$, width $B_{bank}$ and heightover the along-bank axis $h_{bank}$ (not shown), and two bank ends, each with length $L_{end}$. The main part is Gaussian-shaped over the cross-section and the bank ends are in both horizontal directions. Hence, the bank contour is shown at height $0.46 \times h_{bank}$. $\theta_{bank}$ denotes the bank orientation.

### 2.5 Initial topography

The initial topography in this study consists of a single isolated Gaussian-shaped bank in the middle of the domain (Fig. 3). We divide the bank in a main part, with length $L_{bank}$, width $B_{bank}$ and height $h_{bank}$, and two bank ends, each with length $L_{end}$ (Fig. 4). The main part has a Gaussian-shaped cross-section $A_{bank}$ such that $A_{bank} = B_{bank}h_{bank}$. The bank ends have a 2D Gaussian shape such that $V_{tot} = L_{tot}B_{bank}h_{bank}$. Herein, $V_{tot}$ is the total bank volume and $L_{tot} = L_{bank} + 2L_{end}$ is the total bank length. We define $L_{end}$ equal to $0.3B_{bank}$ in order to retain the slope ratio between both horizontal direction in case of bank scaling. The whole bank rotated anticlockwise with respect to the principal tidal current according to bank orientation $\theta_{bank}$.

## 3 Solution procedure

### 3.1 Outline

The solution procedure consists of five steps (Fig. 5). First, we will write the topography $h(x,y)$ as the sum of a spatially uniform $h_0$ and a spatially non-uniform part $h_1$ in section 3.2. Both parts are connected via expansion parameter $\varepsilon$. Secondly, vorticity $\eta$ will be introduced in section 3.3 to formulate the problem compactly. Thirdly, we introduce the hydrodynamic solution vector $\phi = (\eta, u, v, \zeta)$, which will be expanded in powers of $\varepsilon$ in section 3.4. Finally, the sediment fluxes will be obtained directly via a bed load transport formulation from the hydrodynamic solution and bed evolution will be computed via discrete fourth order Runge-Kutta time-stepping of the tidally averaged sediment fluxes in section 3.5. This will serve as input in the next time-step. Additionally, we will present a model version with linearised sediment transport in section 3.6. This is to be applied when nonlinear hydrodynamic contributions are neglected.

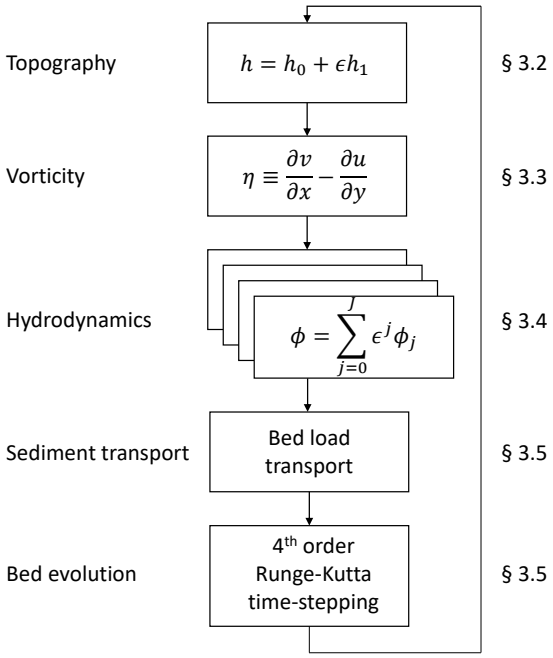


**Fig. 5** Outline of the solution procedure in five steps: (1) the bed is formulated as combination of the flat bed $h_0$ and the perturbed bed $\varepsilon h_1$; (2) vorticity $\eta$ is introduced in the hydrodynamic problem; (3) the hydrodynamic solution $\phi$ is expanded in powers of $\varepsilon$. $j$ and $J$ are respectively the order and the truncation number of the expansion; (4) sediment transport is computed via a bed load transport formulation; (5) the bed level is updated using fourth order Runge-Kutta time-stepping. This is input for the next time step.

### 3.2 Perturbed topography

The topography $h(x,y)$ is formulated as a composition of the mean water depth $h_0$ and the spatially dependent perturbed water depth $h_1$:

$$h = h_0 + \varepsilon h_1 \tag{14}$$

with $\varepsilon$ being an expansion parameter equal to the amplitude of the most perturbed mode ($h_{1max}$) in its truncated Fourier series. This generally equals the bank amplitude. The truncated Fourier series of $h_1$ are written as:

$$h_1(x,y) = \sum_{m=-M}^{M} \sum_{n=-M}^{M} \hat{h}_{1mn}(t) \exp(i[k_m x + l_n y]) \,. \tag{15}$$

Here, the wave numbers associated with domain size $(k_m, l_n) = (m,n)k_{min}$ are introduced, in which $k_{min} = \frac{2\pi}{L_{dom}}$. This formulation complies with the periodic boundaries. Furthermore, $M$ is the spatial truncation number.

### 3.3 Vorticity

Vorticity $\eta$ is defined as

$$\eta \equiv \frac{\partial v}{\partial x} - \frac{\partial u}{\partial y}. \tag{16}$$

An evolution equation for this quantity is obtained by cross-differentiation of the momentum equations (6)-(7) and application of the continuity equation (8). This leads to

$$\mathscr{L}\eta = \underbrace{\left[\frac{f}{h}\frac{\partial h}{\partial x} - \frac{r}{h^2}\frac{\partial h}{\partial y}\right]}_{R} u + \underbrace{\left[\frac{f}{h}\frac{\partial h}{\partial y} + \frac{r}{h^2}\frac{\partial h}{\partial x}\right]}_{S} v \tag{17}$$

with operator $\mathscr{L} = \frac{\partial}{\partial t} + u\frac{\partial}{\partial x} + v\frac{\partial}{\partial y} + \frac{r}{h}$. The vorticity on the left-hand side experiences acceleration, advection and dissipation due to bottom friction. It is produced on the right-hand side by the Coriolis and frictionally induced tide-topography interactions in $x$- and $y$-direction (denoted by $Ru$ respectively $Sv$).

### 3.4 Hydrodynamic solution

The hydrodynamic solution is expanded in powers of $\varepsilon$ according to

$$\phi = \sum_{j=0}^{J} \varepsilon^j \phi_j = \phi_0 + \varepsilon\phi_1 + \varepsilon^2\phi_2 + \ldots + \varepsilon^J\phi_J. \tag{18}$$

Herein, $j$ depicts the order of expansion. We distinguish $j = 0$, $j = 1$ and $j \geq 2$, which represent respectively the contributions of the basic flow, first order flow and higher order flow solutions. The basic flow describes flow over a flat bed, the first order flow the linear flow response to the bed and the higher order flow the nonlinear flow response to the bed. We terminate the hydrodynamic expansion either at a prescribed order $J$ or when the estimations of the functions $S$ and $R$ (see section 3.3) deviate less than $10^{-5}$ from the exact value.

It follows from the expansion that, at each order $j$, the hydrodynamic problem in terms of vorticity is a linear problem forced by the lower order flow solutions. Hence, we start by solving the basic flow and expand its solution towards higher orders. Details of this expansion can be found in the appendices. Appendix B covers the basic flow solution, appendix C covers the first order flow solution and appendix D covers the higher order flow solutions.

### 3.5 Sediment transport and bed evolution

Once the hydrodynamic solution is known to a prescribed order $J$, we will use the truncated flow velocity vector

**Table 1** Overview of dimensions of the initial topography for sample cases A and B and a range for the sensitivity analysis.

| Bank dimension | Symbol | A | B | Range | Unit |
|---|---|---|---|---|---|
| Bank height | $h^*_{bank}$ | 4 | 4 | −4 - 12 | m |
| Bank length | $L^*_{bank}$ | 20 | 10 | 10 - 40 | km |
| Bank width | $B^*_{bank}$ | 2 | 2 | 1 - 4 | km |
| Bank orientation | $\theta_{bank}$ | 0 | 42 | 0 - 360 | deg |

$$\vec{u} = (u, v) = \sum_{j=0}^{J} \varepsilon^j (u_j, v_j) \tag{19}$$

as input for the sediment transport model in Eq. (9), which yields $\vec{q}$ or, in Fourier space, $\hat{\vec{q}}_{mn}$ for each spatial mode $(m,n)$. Eq. (10) is applied to obtain an expression for the bed evolution, which is based on the tidally averaged sediment fluxes according to

$$\frac{\partial \hat{h}_{1mn}}{\partial t_{mor}} = \underbrace{ik_m\langle \hat{q}_{x,mn}\rangle + il_n\langle \hat{q}_{y,mn}\rangle}_{\hat{B}_{mn}}. \tag{20}$$

Herein, we have defined the tide-averaged bed evolution function $B$, which is the morphodynamic response to input topography $h$. The tidal averaging is carried out numerically over $N_{tide}$ equidistant time points in the tidal cycle. Morphodynamic time-stepping is conducted via the fourth order Runge-kutta method. Updating the bed topography effectively closes the morphodynamic loop.

### 3.6 Linear dynamics

In case $J = 1$, implying linear dynamics, we linearise the sediment transport model (following e.g. Hulscher et al 1993):

$$\vec{q} = (|\vec{u_0}|^2 + \frac{1}{2}U_w^2 h_0^{-\kappa})(\vec{u_1} + \lambda'\vec{\nabla}h_1) + (2(\vec{u_0}\cdot\vec{u_1})) - \frac{1}{2}\kappa . U_w^2 h_0^{-\kappa-1} h_1 \vec{u_0} \tag{21}$$

With respect to the bed evolution, we apply the property that there is no interaction between the spatial modes and combine this with Exner's equation (10) to find a formulation in which each mode grows or decays exponentially according to

$$\hat{h}_{1mn}(t_{mor}) = \hat{h}^{init}_{1mn} \exp(\omega_{mn} t_{mor}) \tag{22}$$

with complex growth rate $\omega_{mn} = \frac{\vec{\nabla}\cdot\langle\vec{q_1}\rangle}{\hat{h}_{1mn}}$.

**Table 2** Overview of physical parameters.

| Parameter | Symbol | Value | | | Unit |
|---|---|---|---|---|---|
| Mean water depth | $H^*$ | 25 | | | m |
| Latitude | $\varphi$ | 51 | | | deg |
| Friction coef. | $c_d$ | $2.5 \times 10^{-3}$ | | | – |
| Sediment transport coef. | $\alpha^*$ | $4 \times 10^{-5}$ | | | $s^2\ m^{-1}$ |
| Bed slope coef. | $\tilde{\lambda}^*$ | 2 | | | – |
| Wave stirring parameter | $U_w^*$ | 0.6 | | | $m\ s^{-1}$ |
| Wave stirring power | $\kappa$ | 2 | | | – |
| | | $M_0$ | $M_2$ | $M_4$ | |
| Tidal flow (ampl.) | $\gamma^*_{tide}$ | 0 | 0.6 | 0 | $m\ s^{-1}$ |
| Inclination | $\vartheta_{tide}$ | 0 | 0 | 0 | deg |
| Eccentricity[#] | $\varepsilon_{tide}$ | – | 0 | 0 | – |
| Phase | $\psi_{tide}$ | – | 0 | 0 | deg |

[#] Eccentricity is defined as the ratio of the semiminor and semimajor axis of the tidal ellipse.

**Table 3** Overview of numerical parameters.

| Parameter | Symbol | Value | Unit |
|---|---|---|---|
| Spatial truncation number | $M$ | 128 | – |
| Temporal truncation number | $P$ | 5 | – |
| Calculation points within tidal cycle | $N_{tide}$ | 64 | – |
| Domain length | $L^*_{dom}$ | 100 | km |
| Morphodynamic time step | $\Delta t_{mor}$ | 0.01 | – |

## 4 Results

### 4.1 Overview of simulations

We present two sample cases that feature qualitatively different behaviour. The cases differ only in their initial topography. All physical and numerical parameters are equal. Furthermore, we will investigate the sensitivity of the plan view evolution to a varying initial topography. The dimensions and their range to be varied for the sensitivity analysis are listed in Table 1. All runs are executed under North Sea conditions. The physical parameters are listed in Table 2 and the numerical settings are listed in Table 3.

### 4.2 Sample case A

*Plan-view evolution* The plan view evolution of a bank parallel to the principal tidal flow is investigated as sample case A. This choice relates to the initial stage in Caston (1972) [Fig. 1]. In the evolution according to our model, we distinguish four characteristic stages (Fig. 6a-d):

(a) The initial topography consists of a bank height of 4 m, bank length of 20 km, bank width of 2 km and an orientation parallel to the principal tidal flow. These dimensions correspond to $\varepsilon = 0.16$.

(b) The ends rotate anticlockwise towards the preferred angle of deposition. Furthermore, the bed parallel to the head and the tail deepens, which results in the formation of parallel troughs and bank with yet a small amplitude. We also find erosion over the whole bank, but especially at the central part. This results in an S-shaped topography with rotated crests at both ends of the bank and a slightly lower central part.

(c) The elevated crests grow in amplitude and length, while the central part continues to erode. This results in two separate growing features.

(d) The central depression turns into a trough, which breaks the original bank in two parts. The separate banks align towards a field of sandbanks. All features grow in amplitude and elongate. This includes the two main banks, troughs and newly formed parallel banks (stage b).

*Hydrodynamics* The underlying hydrodynamics of each stage are provided in the middle and bottom row of Fig. 6 in the form of streamlines (middle row) and flow divergences (bottom row). The streamlines are computed by stream function $\Psi$, which satisfies

$$\frac{\partial \Psi}{\partial y} = hu\,, \qquad \frac{\partial \Psi}{\partial x} = -hv\,. \tag{23}$$

Furthermore, the flow divergences $\vec{\nabla} \cdot \vec{u}$ show zones of convergence and divergence.

We observe clockwise circulation of the residual flow around the bank at all stages. In stages (a) and (b), the circulation occurs around the whole bank and is skewed towards the preferred angle of deposition. Furthermore, anticlockwise rotation cells are present at the locations where troughs form. All streamlines converge at the ends of the banks. This corresponds with the location of the largest flow acceleration and deceleration (where the streamlines diverge).

In stage (c), separate clockwise circulation cells are present around both elevated crests, which are stronger than the circulation around both banks. The anticlockwise circulation around the trough is also strengthened. The more complex streamline pattern results in additional zones of flow acceleration and deceleration. Acceleration occurs at the bank ends and over the central part of the bank and deceleration occurs around the elevated crests. Finally, the anticlockwise circulations have disappeared in stage (d), while the flow divergence field shows acceleration at the far ends of the banks and deceleration at sides facing the $x$-axis.

### 4.3 Sample case B

*Plan-view evolution* Sample case B is subject to the same physical conditions as sample case A, but differs in initial topography. It has an anticlockwise orientation (with respect to the principal tidal flow) and is shorter than case A. This initial topography relates to Huthnance (1982b) and Smith (1988) [Fig. 2]. The plan view evolution is presented in Fig. 7. We again distinguish four stages:

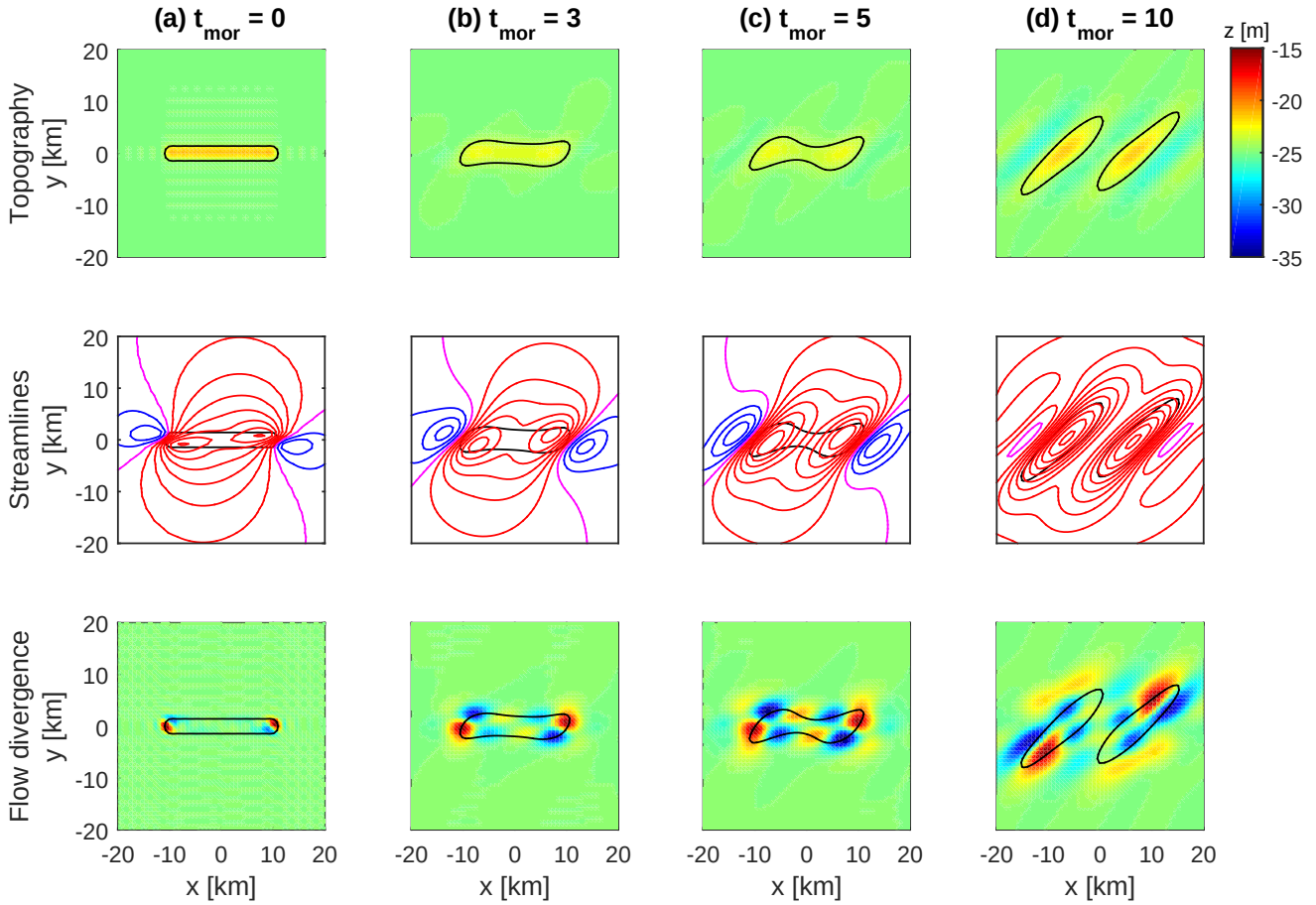


**Fig. 6** Dynamics of sample case A at four evolution stages: (a) $t_{mor} = 0$, (b) $t_{mor} = 3$, (c) $t_{mor} = 5$ and (d) $t_{mor} = 10$ with $\Delta t_{mor} = 235$ year. The top row show the plan view evolution. The middle row shows streamlines $\Psi$ of the residual flow (red clockwise, blue anticlockwise). The bottom row shows flow divergences of the residual flow (red acceleration, blue deceleration). The stages are explained in text. Note that the plotting domain is only a part of the model domain. Contour lines correspond with $z = -24$ m.

(a) The initial topography consists of a bank with a height of 4 m, length of 10 km, width of 2 km and an orientation of 42 degrees anticlockwise with respect to the principal tidal current. This angle is obtained from the fastest growing mode in the linear model (section 3.6).

(b) The bank retains its straight outline, but the central part of the bank grows faster than the bank ends. We also observe the formation of troughs adjacent to the bank.

(c) The bank grows in amplitude and elongates. The fastest growth is observed at the central part of the bank. Further pattern expansion is suppressed.

(d) The central part of the bank rotates clockwise towards an orientation parallel to the principal tidal flow, while the ends remain oriented towards the preferred angle of deposition. The bank outline is now S-shaped.

Contrary to sample case A, the initial bank does not break. Major differences are the rate and location of growth. Sample case B grows faster in amplitude and length than case A. Furthermore, sample case B shows central growth, while case A grows at the bank ends. Similarities can be found in their preferred orientation in stage (a-c) and their tendency to expand their pattern. Although, the latter is suppressed in sample case B during the later stages.

*Hydrodynamics* The hydrodynamics are presented on the middle and bottom row of Fig. 7. The middle row shows the streamlines for all stages and the bottom row the flow divergences. We observe elliptic clockwise rotations around the bank at all stages. The major axis of the ellipse rotates clockwise over time. Its orientation is anticlockwise of the initial bank orientation at stage (a), but parallel to the bank and the principal tidal flow in stage (d). The residual flow velocities are the highest at the slopes of the central part of the bank, where the distances between the streamlines are the smallest.

The residual flow divergences are consistent over all stages. The flow decelerates over bank slopes facing the $x$-axis and accelerates over bank slopes not facing the $x$-axis. In stage (c) and (d), maximum flow acceleration and deceleration occur over the inner and outer bend of the S-shape respectively.

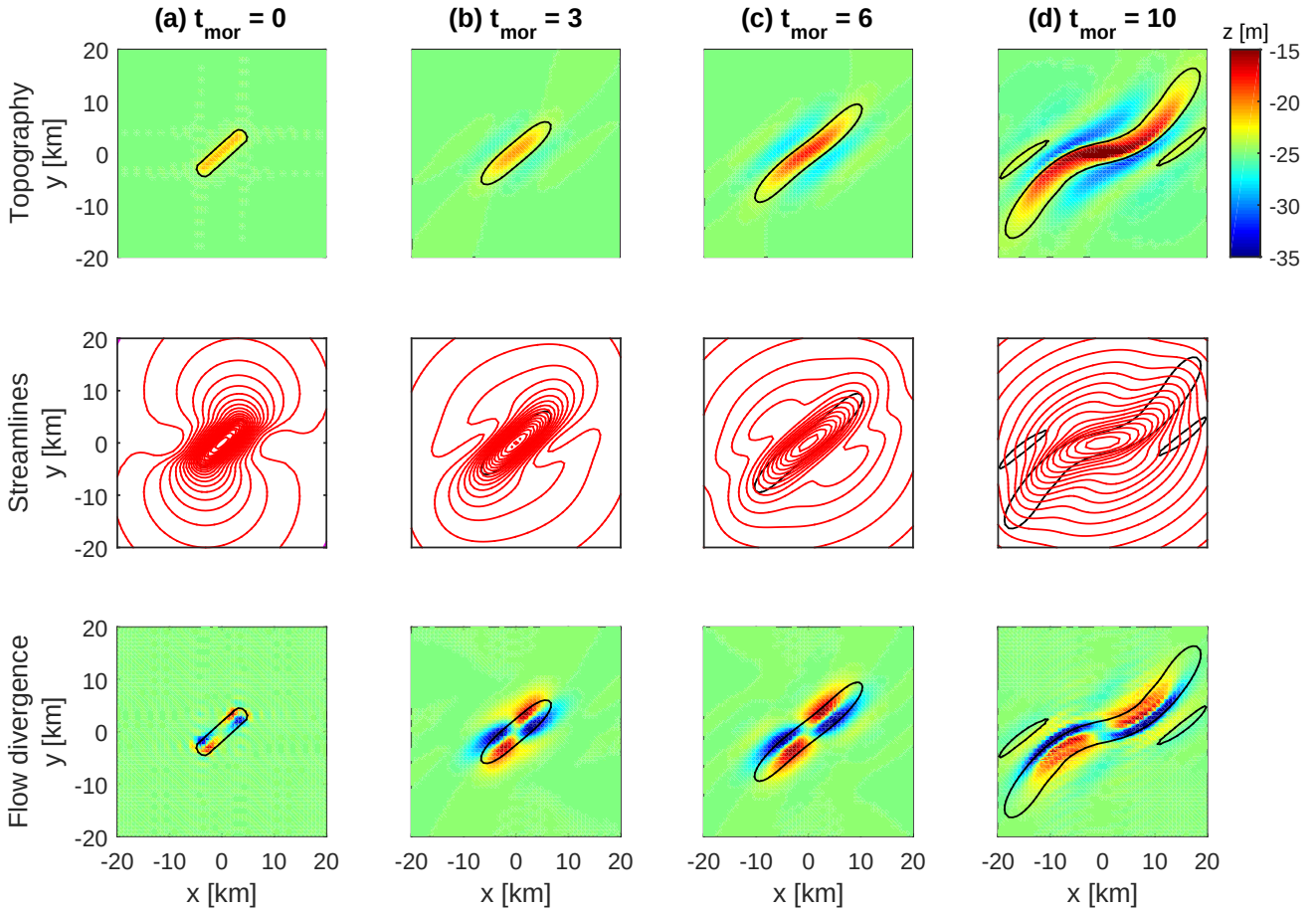


**Fig. 7** Dynamics of sample case B at four evolution stages: (a) $t_{mor} = 0$, (b) $t_{mor} = 3$, (c) $t_{mor} = 5$ and (d) $t_{mor} = 10$ with $\Delta t_{mor} = 235$ year. The top row show the plan view evolution. The middle row shows streamlines $\Psi$ of the residual flow (red clockwise, blue anticlockwise). The bottom row shows flow divergences of the residual flow (red acceleration, blue deceleration). The stages are explained in text. Note that the plotting domain is only a part of the model domain. Contour lines correspond with $z = -24$ m.

### 4.4 Sensitivity to initial topography

Here, a sensitivity analysis will be performed to identify how the plan view evolution depends on the initial topography, while keeping flow conditions. We investigate the effect of the following characteristics of the initial topography: orientation $\theta_{bank}$ (with respect to the principal tidal current), bank length $L_{bank}$, bank height $h_{bank}$ and bank width $B_{bank}$.

*Orientation* The initial orientation $\theta_{bank}$ of the bank with respect tot the principal tidal controls the type of evolution (Fig. 8). Five orientations have been examined: (1) a bank parallel to the principal tidal flow (short version of sample case A, top row), (2) a bank oriented 20 degrees anticlockwise (second row) (3) a bank oriented in the preferred angle of deposition (sample case B, third row), (4) a bank perpendicular to the principal tidal flow (fourth row); (5) a bank perpendicular to the preferred angle of deposition (bottom row). All banks have a length of 10 km, because the characteristic dynamics of each orientation are best shown at this bank length.

All orientations show the strongest topographic changes at their bank ends, which prefer an orientation in the direction of the angle of preferred deposition. For each orientation, this results in a different shape. The parallel case takes an S-shape, the 20 degree case rotates slightly anticlockwise as a whole, the preferred angle case retains its shape, the perpendicular case takes a Z-shape and the perpendicular to the preferred angle case takes an H-shape. The perpendicular case and the perpendicular to the preferred angle case eventually break due to separate evolution of the elevated crests (similar to sample case A). For the perpendicular case this is characterized by a depression, which remains constant at 3 metres above mean bed level, rather than a trough. Its pattern expansion is also limited. The perpendicular to the preferred angle case does form a trough and aligns towards a sandbank field. These properties are also observed in sample case A. This case is also the quickest in its breaking process.

Contrary to sample case A, the parallel case does not break. This indicates an effect of the initial bank length, which will be discussed in the next paragraph. The angle

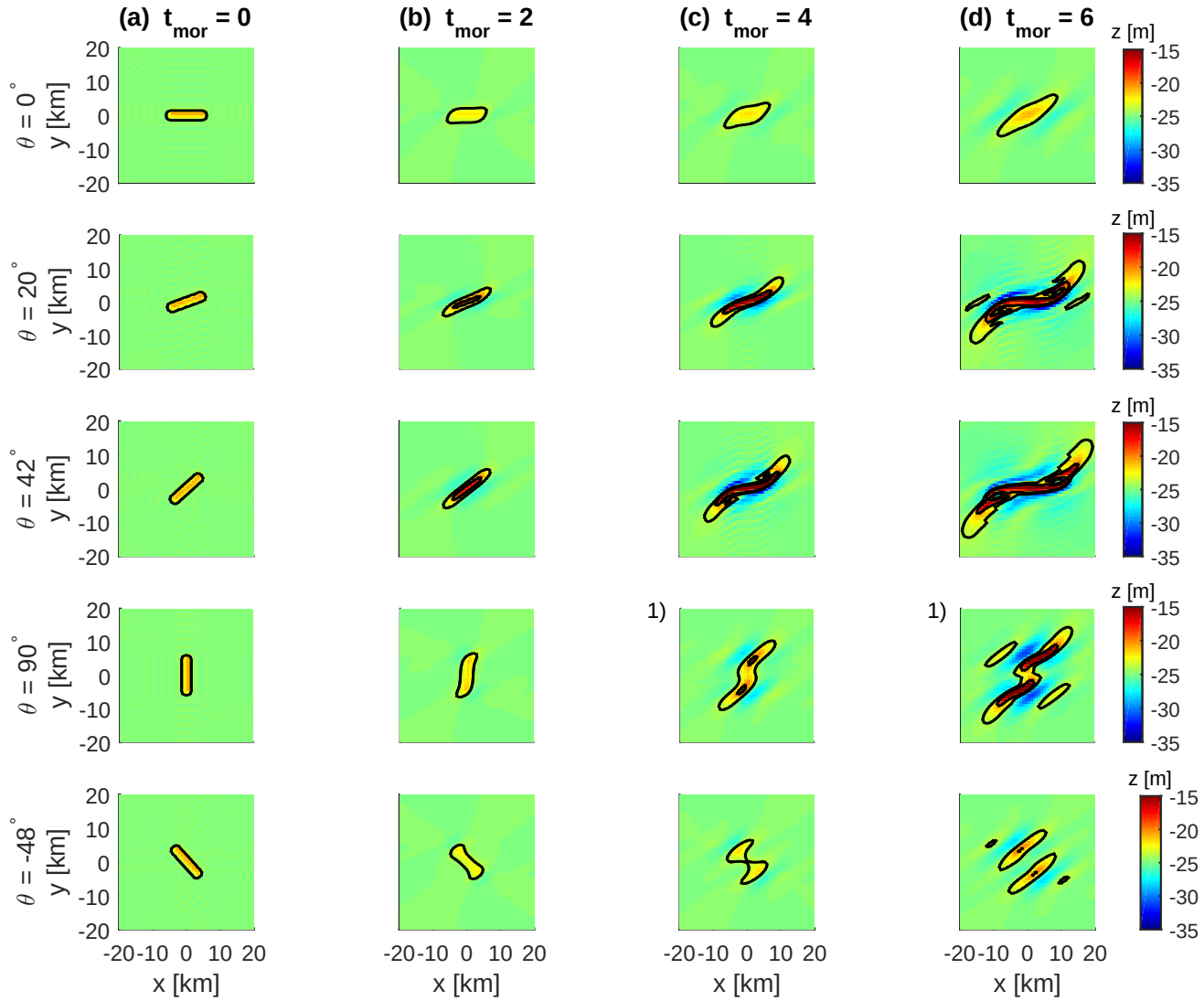


**Fig. 8** Sensitivity of the initial orientation with respect to the principal tidal flow. From top to bottom row: parallel (0° anticlockwise), slightly rotated (20°), angle of preferred deposition (42°), perpendicular (90°), perpendicular to angle of preferred deposition (-48°). Contour lines correspond with $z = -24$ and $z = -20$ m. [1)] The perpendicular case is presented at $t_{mor} = 5$ for stage (c) and at $t_{mor} = 7$ for stage (d) to highlight its bank-breaking dynamics. [2)] These analysis have been carried out with $\gamma_{tide} = 0.7$ m/s. To be fixed before submission to Ocean Dynamics.

of preferred deposition case equals sample case B and its dynamics were thoroughly discussed in section 4.3. Banks with an initial orientation between the parallel and the preferred angle cases follow one these. The 20 degree case follows the evolution of the preferred angle case, while a bank with an anticlockwise orientation of 10 degrees follows the evolution of the parallel case (not shown in Fig. 8).

*Bank length* The initial bank length $L_{bank}$ controls the number of separate banks in which the initial bank will break. Banks with initial lengths of 10, 20 and 40 kilometres have been investigated for both sample cases (not shown). Sample case A had a bank length of 20 km and broke into two parts. The 10 km bank does not break. Compared to the 20 km case, the ends indeed rotate towards the angle of preferred deposition, but the two elevated crests grow too close to each other and eventually reconnect. This results in a bank with a very wide central kink, where it grows the fastest. Ultimately, the central part also rotates towards the angle of preferred deposition and this case continues to evolve similarly to sample case B, but with additional pattern expansion.

On the other hand, the head and the tail develop far apart in the 40 km case. As a result, two separate bank fields develop and those do not interact. The remaining central part develops into a separate bank, which rotates towards the angle of fastest deposition and grows after an initial decay, but it lags far behind the two sandbank fields in both sides. Sample case B does not break for any bank length.

*Bank height* The initial bank height $h_{bank}$ controls the extent to which patterns expansion occurs and may as well affect the time scale of the dynamics. We varied the initial

bank height with values of 2 and 8 meters and a 4 meter deep pit, which were compared to a height of 4 meters of the sample cases. Furthermore, we looked at a perpendicular bank with a height of 8 m. Interestingly, all banks evolve similar to their respective sample case. However, we find that the pit cases trigger the most parallel banks and troughs, while less are triggered by initially higher banks. For sample case B, we also find that these bank evolve faster towards an S-shape, but the bank-breaking time scale is unaffected for sample case A. On the other hand, the breaking time scale was reduced for the 8 m perpendicular bank. These differences indicate that height effects are closely related to the type of evolution.

*Bank width* The initial bank width $B_{bank}$ controls the rate of amplitude growth and affects the bank dimension on longer time scales. The bank width is varied to values of 1 and 4 kilometer. Both banks show qualitatively similar behaviour as the sample cases. The main difference is that the 4 km banks enhance amplitude growth, while it is weakened for the 1 km banks. However, literature indicates that further widening may not necessarily strengthen amplitude growth, because there will be a preferred wave length (e.g. Hulscher et al 1993).

Additionally, the 4 km banks remain wider at all stages, while the 1 km banks remain smaller. However, the difference with respect to the sample cases tends to decrease over time. Especially the 1 km bank tends to widen.

### 4.5 Other sensitivities

- Flow velocity $\gamma_{tide}$ (velocity amplitude of the $M_2$-tide) affects the time scale of the evolution. Higher flow velocities result in a faster evolution time scale. This relation is stronger than the cubic relation in the bed load transport formula (Eq. 4).
- The wave stirring parameter $U_w$ damps the topography and as such affects the bank outline as well as the time scale of the dynamics. A higher wave stirring parameter flattens the bank slopes, increases bank width and suppresses amplitude growth.
- Exclusion of Coriolis, i.e. $f = 0$, results in a second preferred angle of deposition, which is mirrored over the $x$-axis. Hence, the bank ends in sample case A rotate in both directions, which results in a cross-shaped plan view at both ends and breaking into multiple small banks. Sample case B is already oriented in the original preferred angle and thus unaffected.
- Bottom friction is essential for the production of Coriolis, which controls the time scale of evolution. An increased bottom friction coefficient $c_d$ strengthens amplitude growth and quickens breaking and evolution towards an S-Shape.
- The sediment transport coefficient $\alpha$ is inversely proportional to the time scale of evolution. This coefficient incorporates the effects grain size, sediment density and critical shear stress parameter.
- The porosity $\varepsilon_{por}$ controls the time scale of evolution. A higher porosity results in a faster evolution.

## 5 Discussion

### 5.1 Classification of bank evolution paths

Based on the results and sensitivity analysis, we classify the plan view evolution of the banks in three general paths (Fig. 9). Each path can be divided in four stages. The followed path depends on initial orientation and initial bank length.

*Path:* (I) Initial topography → (II) Rotation of the bank ends → (III) Separate growth → (IV) Bank breaking

All breaking banks, such as sample case A, follow this path. It requires a sufficiently long initial bank length and an initial orientation not in the direction of the preferred angle of deposition. Path characteristics are rotation and separate evolution of the bank ends, resulting in various forms of breaking. Parts can be separated by troughs (e.g. sample case A) or depressions (e.g. the perpendicular case), and, depending on initial orientation and bank height, may align in various configurations such as a sandbank field or a head-tail connection. Finally, the number of separate banks depends on the bank length. The proposed path differs with the stages in Caston (1972), while the evolution described in Smith (1988) complies with (III) → (IV) on this path. The relation to Caston (1972) and Smith (1988) will be covered in section 5.4.

*Path:* (I) Initial topography → (II) Rotation of the bank ends → (III) Central growth → (IV) S-shape

This path is followed by banks with an initial orientation not in the direction of the preferred angle of deposition and an initial bank length, which is too short for breaking. An example is the short version of sample case A (Fig. 6, top row). The path is characterised by rotation of the bank ends followed by central growth and evolution towards an S-shape. There is no separate evolution of the bank ends, because they are not far enough apart.

*Path:* (I) Initial topography → (II) Straight bank → (III) Central growth → (IV) S-shape

This path is followed by banks with an initial orientation in, or close to, the direction of the preferred angle of deposition, such as sample case B. It is characterised by a

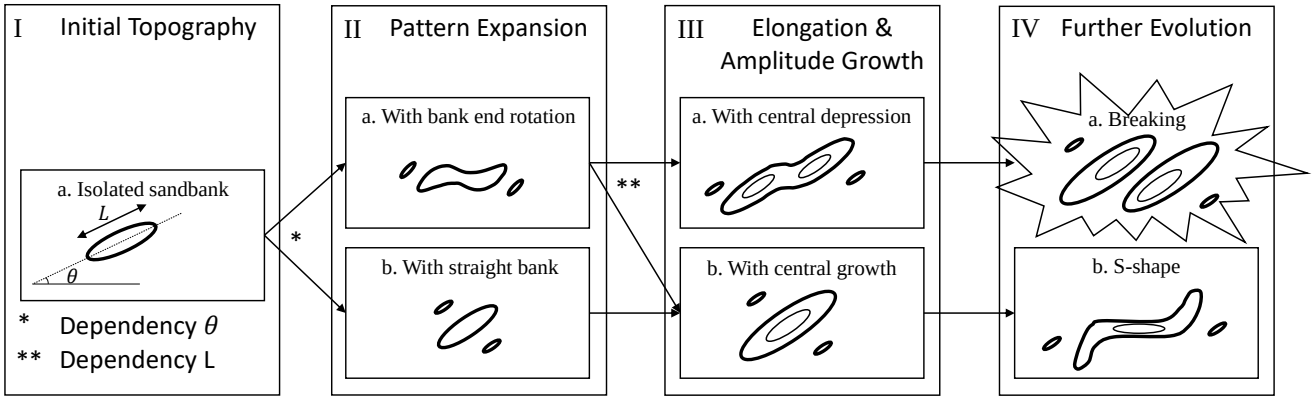


**Fig. 9** General flow chart of possible bank evolution mechanisms. We distinguish three paths: (A) Initial topography → Rotation of the ends → Separate growth → Breaking; (B) Initial topography → Rotation of the ends → Central growth → S-shape; (C) Initial topography → Straight bank → Central growth → S-shape. The followed path depends on initial orientation and bank length.

straight bank with central growth followed by clockwise rotation of the central part towards a direction parallel to the principal tidal flow. This results in a characteristic S-shape. Huthnance (1982b) presents a model result with a similar path. This is covered in section 5.4.

In addition to the path-specific dynamics, banks are also subject to path-independent dynamics. These are pattern expansion during stage (II) and elongation and amplitude growth during stage (III). Finally, we emphasize that these are general paths and specific evolution depends on the topographic and physical properties.

## 5.2 Physical description

We describe the physics along path stages II to IV. Stage I is model input and therefore left out.

Stage II is characterized by pattern expansion and possible rotation of the bank ends. Both sample cases and the sensitivity analysis have shown that the initial orientation controls whether the bank ends rotate. If the initial orientation is in its preferred angle, no rotation occurs. If this is not the case, the ends rotate towards the preferred angle of deposition. This is driven by linear process as described by, among others, Huthnance (1982a) and Robinson (1983). The rotation occurs at the end, because the middle part cannot drive a divergence in sediment transport. Pattern expansion is also explained by these linear processes (e.g. Roos et al 2008). We add that the expansion rate is suppressed for fast growing banks.

Stage III is characterized by elongation and amplitude growth, which can occur at the ends of the bank (IIIa) or at the central part of the bank (IIIb). We find that banks without rotated ends always show central growth, while it depends on the initial bank length for banks with rotated ends. Those show separate growth when the bank is sufficiently long, but central growth otherwise. Amplitude growth is driven by the generation of vorticity under an oblique angle (similar to linear processes), while elongation is the result of decelerating currents and decreasing net transport when they turn around the bank end with net deposition (Huthnance 1982b).

Stage IV is the result of the continued evolution of the previous stages. This results in bank-breaking or an S-shaped plan view. Our simulations indicate that the broken banks may also form an S-shape over longer time, but our simulations have been to short too conclude this. We explain breaking as the result of separately evolving bank ends combined with central erosion. The characteristic S-shape is explained as the combination of three effects: (1) when the bank grows, the depth over the bank decreases. Consequently the friction term, which prefers a parallel orientation of the along-bank axis with respect to the principal tidal flow, increases in weight relatively to the Coriolis term in the vorticity equation (17); (2) the residual currents converge parallel to the middle part of the bank instead of the bank ends (Fig. 7); (3) residual flow accelerates over slopes facing the $x$-axis and decelerates over slopes not facing the $x$-axis. The combination of these three effects drives rotation of the central part of bank towards an orientation parallel to the principal tidal flow.

## 5.3 Linear versus nonlinear dynamics

Our model includes both linear and nonlinear dynamics. Each contributes to the plan view evolution in its own way (Fig. 10-11). The linear contribution (section 3.6) drives rotation of the bank ends, amplitude growth and pattern expansion in accordance with the fastest growing mode. This is the spatial mode that dominates the linear topography over time (Dodd et al 2003). Under the physical conditions of the sample cases, this mode has a wave length of 7.9 km and an

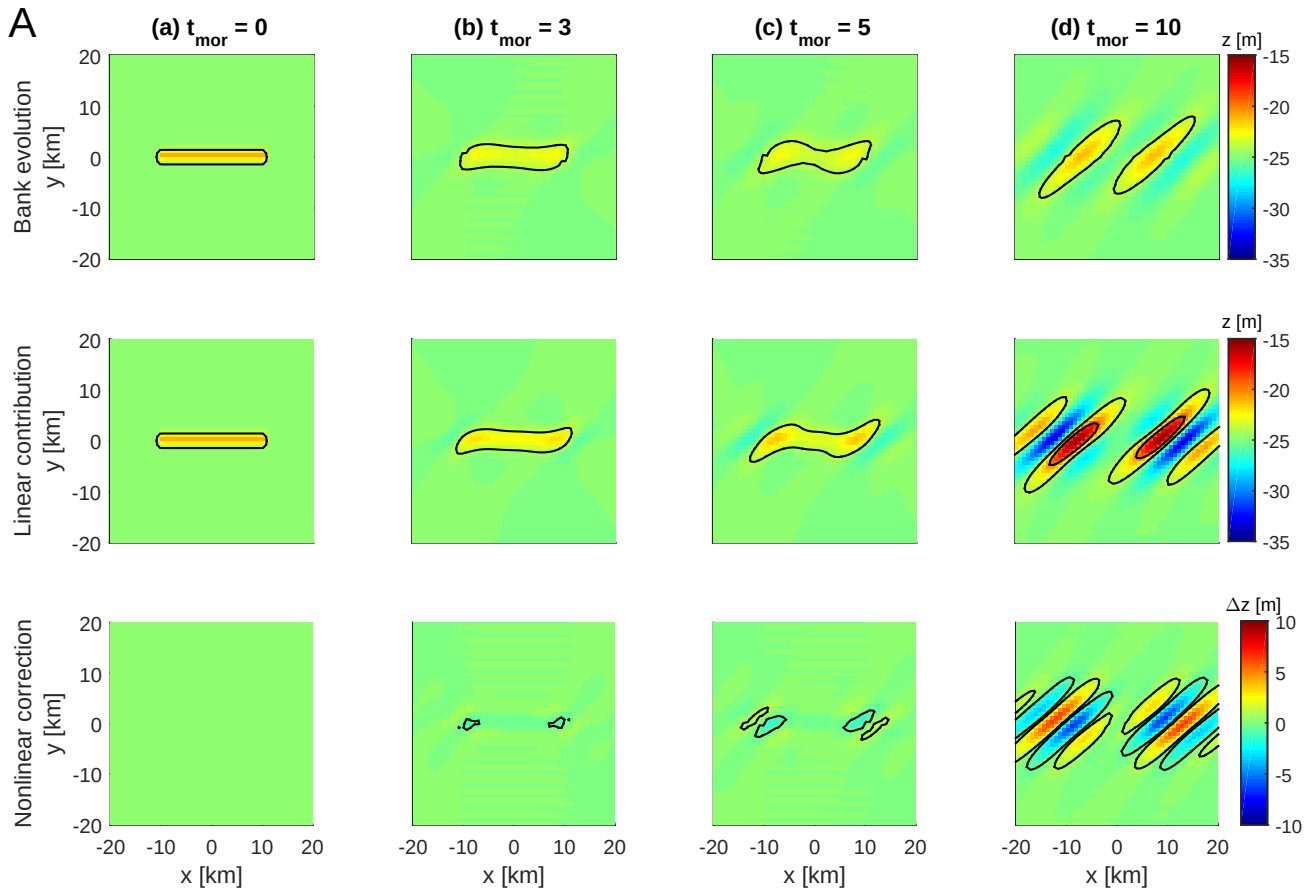


**Fig. 10** Comparison of linear and nonlinear effects on the plan view evolution of sample case A. Top row: modelled plan view evolution. Middle row: plan view evolution based on linear dynamics only. Bottom row: nonlinear correction terms. Contour lines are at $z = -24$ and $z = -20$ m in the top two rows and at $\Delta z = 0.75$ and $\Delta z = -0.75$ m in the bottom row.

orientation of 45 degrees anticlockwise with respect to the principal tidal current.

The nonlinear contributions damp amplitude growth and pattern expansion and drive evolution towards an S-shape. The damping effects can clearly be seen in sample case A (Fig. 10, bottom row). There is a positive contribution to the bed levels at troughs, while it is negative at crests. This is consistent with the observation that pattern expansion is suppressed for initially higher banks, for which the nonlinear contribution is relatively stronger.

Sample case B (Fig. 11, bottom row) shows the production of an S-shape next to the damping effects. This can most clearly be seen by the asymmetry of the positive correction terms in stages (c) and (d). These are wider in the top-right and bottom-left quadrants in stage (c) as well as longer in stage (d). Hence, rotation of bank ends and pattern expansion can also be captured in a linear model, but the suppression of pattern expansion and the S-shape require the inclusion of nonlinear dynamics.

### 5.4 Comparison with bank-break hypotheses from literature

The breaking mechanism as proposed by Caston (1972) [Fig. 1] is related to sample case A. Both plan view descriptions show a parallel bank that breaks in response to tidal flow. We were able to reproduce breaking in three parts by lengthening the initial profile. However, his intermediate stages do not fit our path.

The breaking mechanism of an oblique bank as proposed by Smith (1988) [Fig. 2] related to sample case B, but could only be reproduced with a different initial topography. Sample case B lacked a necessary kink. Instead, such instability was found in the evolution of a perpendicular bank (Fig. 8, fourth row). After rotation of the bank ends, stage (III) shows an oblique bank with a kink, which corresponds with the initial topography in Smith (1988). Hereafter, both describe that the bank breaks, because the head and tail of the separate growing bank ends drift apart.

In his description, Smith (1988) suggests that sandwaves may affect the breaking mechanism. These are driven by circulations in the vertical plane, which would require 3D-model to include (Hulscher 1996). However, while severely

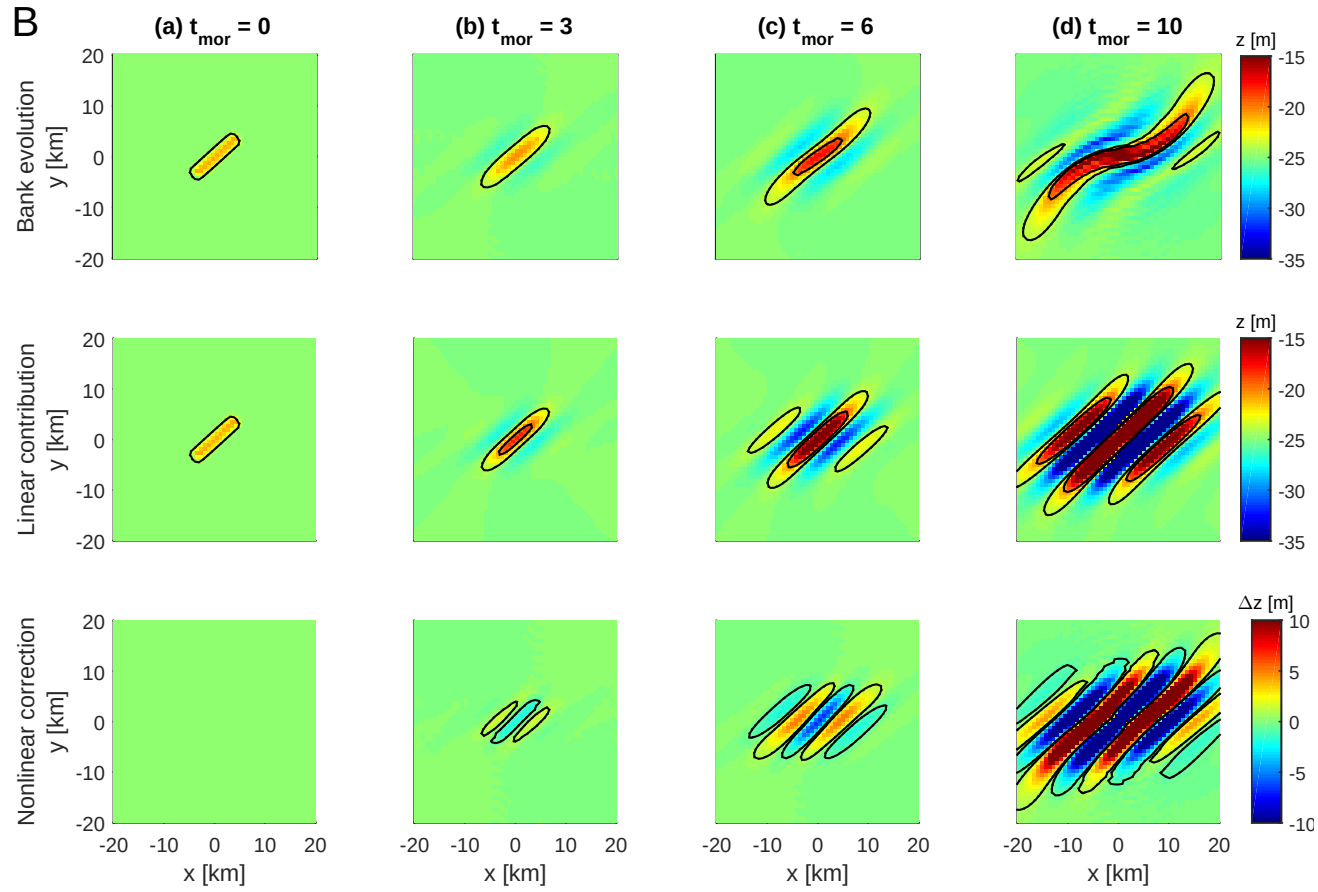


**Fig. 11** Comparison of linear and nonlinear effects on the plan view evolution of sample case B. Top row: modelled plan view evolution. Middle row: plan view evolution based on linear dynamics only. Bottom row: nonlinear correction terms. Contour lines are at $z = -24$ and $z = -20$ m in the top two rows and at $\Delta z = 0.75$ and $\Delta z = -0.75$ m in the bottom row.

increasing the computational load, this may add little to our current model. We have shown that sandwaves are not required for bank-breaking and, moreover, sandbanks are governed by circulations in the horizontal plane. Alternatively, Deleu et al (2004) suggests that tidal flow asymmetry may be required. Although we have presented bank-breaking without tidal asymmetry, it would allow for migration and may affect the breaking mechanism.

The model results from Huthnance (1982b) are very comparable to sample case B. We were able to reproduce the elongation and the characteristic S-shape of the bank. Furthermore, Huthnance (1982b) also investigated a bank perpendicular to the tidal flow. He shows that this indeed leads to the evolution of two separate banks. However, we have shown that, for example for sample case A, Coriolis forces are essential. Furthermore, we use a more advanced flow description. The inclusion of both Coriolis and sinusoidal flow allow for more topographies and better estimates of evolution time scales.

### 5.5 Comparison to North Sea banks

We have shown that banks evolve along three generic paths, but that its specific topography depends on the initial shape and physical conditions. Nonetheless, each evolution paths shows that along-bank irregularities in orientation, width and height are triggered. These along-bank irregularities comply, for example, with the bathymetry of the Norfolk Banks (Fig. 12). The Ower Bank and the Indefatigable banks show a kink in their topography, which we found after rotation of the bank ends at stage (b). Furthermore, the Swarte Bank and the Indefatigable Banks show separately growing features. These were found at stage (c) on our proposed breaking path. Finally, the Leman Bank and Ower Bank show a meandering along-bank profile, which is associated to meandering forms as found on paths triggering an S-shaped topography.

Besides good resemblance to the bathymetry of Norfolk banks, our model has reproduced bank-breaking hypotheses from literature that are based on observations (Caston 1972; Smith 1988).

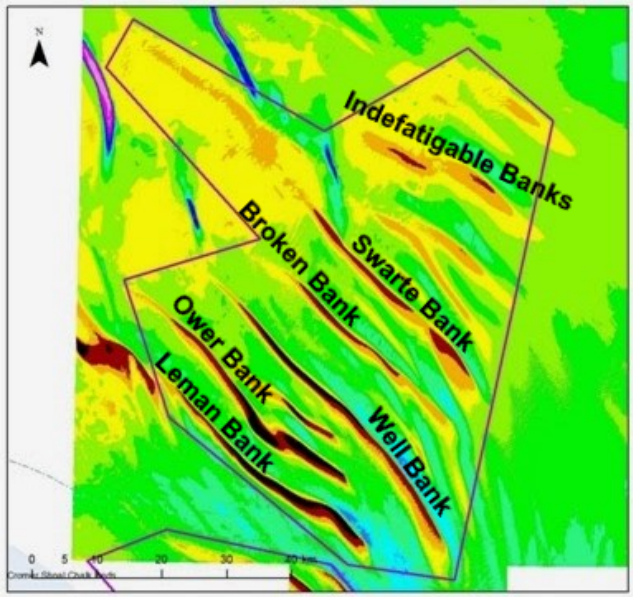


**Fig. 12** Map op the bathymetry of the Norfolk banks, UK Continental Shelf. Red represents the shallowest parts, while blue represents the deepest parts. Data obtained from Carr (2013)

.

## 6 Conclusions

The process-based nonlinear idealized morphodynamic model presented in this research has shown to be capable of describing the transient long-term plan view dynamics of isolated sandbanks with the inclusion of nonlinear interactions between tidal flow, topography, Coriolis and bottom friction, and depth-dependent wind wave stirring in the formulation of the hydrodynamics and slope effects in the formulation of bed-load sediment transport. The nonlinear dynamics prove to be essential as damper and for modelling meandering bed forms.

We distinguish three generic evolution paths. (I) Rotation of the bank ends towards the preferred angle of deposition and separate growth, causing bank-breaking. (II) Rotation of the bank ends towards the preferred angle of deposition and central growth, triggering an S-shape. (III) Straight outline and central growth, triggering an S-shape, but much faster than path II. In addition to the path-dependent dynamics, the banks also experience pattern expansion, elongation and amplitude growth (possibly after initial erosion), which are controlled by (a combination of) initial orientation, height and width.

The followed path depends on the initial bank orientation and length. Bank-breaking (path I) requires two condition. The initial bank orientation may not already be in the angle of preferred deposition. This would prevent the formation of a kink in the middle part of the bank. Furthermore, the bank should be sufficiently long for the elevated crests to develop separately. The bank length also controls the number of parts the bank will break in. If the first condition is not fulfilled, the bank will evolve along path III. If only the second condition is not fulfilled, the bank will develop along path II.

The here presented paths are consistent with the observational-based breaking mechanism by Smith (1988) and the results of the stability model by Huthnance (1982b). Although we were able to reproduce breaking under the conditions in Caston (1972), his stages do not fit our path. Furthermore, in each path, a straight bank triggered along-bank irregularities in orientation, width and height. Such irregularities show resemblance to broken and meandering forms as found in the North Sea.

We have successfully investigated the transient evolution of tidal sandbanks, but a bank will continue to evolve. It is left for future work to extent the paths towards equilibria. Other interesting topics are the effect of (tidal) asymmetries and the evolution starting from a random, infinitesimal perturbed bed.

## References

Atalah J, Fitch J, Coughlan J, Chopelet J, Coscia I, Farrell E (2012) Diversity of demersal and megafaunal assemblages inhabiting sandbanks of the Irish Sea. Mar Biodiv 43(2):121–132, DOI 10.1007/s12526-012-0139-y

Brière C, Roos PC, Garel E, Hulscher SJMH (2010) Modelling the Morphodynamics of the Kwinte Bank, Subject to Sand Extraction. Journal of Coastal Research pp 117–126

Carr H (2013) Site bathymetry showing the distribution of sandbanks

Caston VND (1972) Linaer Sand Banks in the Southern North Sea. Sedimentology 18(1-2):63–78, DOI 10.1111/j.1365-3091.1972.tb00003.x

Caston VND, Stride AH (1970) Tidal sand movement between some linear sand banks in the North Sea off northeast Norfolk. Marine Geology 9(5):M38–M42, DOI 10.1016/0025-3227(70)90018-6

De Vriend HJ (1990) Morphological Processes in Shallow Tidal Seas. In: Cheng RT (ed) Residual Currents and Long-term Transport, no. 38 in Coastal and Estuarine Studies, Springer New York, pp 276–301, dOI: 10.1007/978-1-4613-9061-9_20

Deleu S, Van Lancker V, Van den Eynde D, Moerkerke G (2004) Morphodynamic evolution of the kink of an offshore tidal sandbank: the Westhinder Bank (Southern North Sea). Continental Shelf Research 24(15):1587–1610, DOI 10.1016/j.csr.2004.07.001

Dodd N, Blondeaux P, Calvete D, De Swart HE, Falques A, Hulscher S, Rozynski G, Vittori G (2003) Understanding coastal morphodynamics using stability methods. J Coast Res 19(4):849–866, wOS:000186579700008

Dolphin TJ, Vincent CE, Coughlan C, Rees JM (2007) Variability in Sandbank Behaviour at Decadal and Annual Time-Scales and Implications for Adjacent Beaches. ResearchGate 50:731–737

Dyer KR, Huntley DA (1999) The origin, classification and modelling of sand banks and ridges. Continental Shelf Research 19(10):1285–1330, DOI 10.1016/S0278-4343(99)00028-X

Van den Eynde D, Giardino A, Portilla J, Fettweis M, Francken F, Monbaliu J (2010) Modelling the Effects of Sand Extraction, on Sediment Transport due to Tides, on the Kwinte Bank. Journal of Coastal Research pp 101–116

Fairley I, Masters I, Karunarathna H (2016) Numerical modelling of storm and surge events on offshore sandbanks. Marine Geology 371:106–119, DOI 10.1016/j.margeo.2015.11.007
Horrillo-Caraballo JM, Reeve DE (2008) Morphodynamic behaviour of a nearshore sandbank system: The Great Yarmouth Sandbanks, U.K. Marine Geology 254(12):91–106, DOI 10.1016/j.margeo.2008.05.014
Hulscher SJMH (1996) Tidal-induced large-scale regular bed form patterns in a three-dimensional shallow water model. J Geophys Res 101(C9):20,727–20,744, DOI 10.1029/96JC01662
Hulscher SJMH, de Swart HE, de Vriend HJ (1993) The generation of offshore tidal sand banks and sand waves. Continental Shelf Research 13(11):1183–1204, DOI 10.1016/0278-4343(93)90048-3
Huthnance JM (1982a) On one mechanism forming linear sand banks. Estuarine, Coastal and Shelf Science 14(1):79–99, DOI 10.1016/S0302-3524(82)80068-6
Huthnance JM (1982b) On the formation of sand banks of finite extent. Estuarine, Coastal and Shelf Science 15(3):277–299, DOI 10.1016/0272-7714(82)90064-6
Kaiser MJ, Bergmann M, Hinz H, Galanidi M, Shucksmith R, Rees EIS, Darbyshire T, Ramsay K (2004) Demersal fish and epifauna associated with sandbank habitats. Estuarine, Coastal and Shelf Science 60(3):445–456, DOI 10.1016/j.ecss.2004.02.005
Kenyon NH, Belderson RH, Stride AH, Johnson MA (1981) Offshore Tidal Sand-Banks as Indicators of Net Sand Transport and as Potential Deposits. In: Nio SD, Shttenhelm RTE, Weering TCEV (eds) Holocene Marine Sedimentation in the North Sea Basin, Blackwell Publishing Ltd., pp 257–268
Knaapen MAF (2005) Sandwave migration predictor based on shape information. J Geophys Res 110(F4):F04S11, DOI 10.1029/2004JF000195
Pan S, MacDonald N, Williams J, O'Connor BA, Nicholson J, Davies AM (2007) Modelling the hydrodynamics of offshore sandbanks. Continental Shelf Research 27(9):1264–1286, DOI 10.1016/j.csr.2007.01.007
Pattiaratchi C, Collins M (1987) Mechanisms for linear sandbank formation and maintenance in relation to dynamical oceanographic observations. Prog Oceanograph. Progress In Oceanography 19(2):117–176, DOI 10.1016/0079-6611(87)90006-1
Robinson IS (1983) Tidally Induced Residual Flows. In: Johns B (ed) Elsevier Oceanography Series, Physical Oceanography of Coastal and Shelf Seas, vol 35, Elsevier, pp 321–356
Roos PC, Hulscher SJMH (2003) Large-scale seabed dynamics in offshore morphology: Modeling human intervention. Rev Geophys 41(2):1010, DOI 10.1029/2002RG000120
Roos PC, Hulscher SJMH (2004) Modelling the morphodynamic effects of different design options for offshore sandpits. In: Marine sandwave and river dune dynamics II, University of Twente, Enschede, pp 262–269
Roos PC, Hulscher SJMH, Knaapen MAF, Van Damme RMJ (2004) The cross-sectional shape of tidal sandbanks: Modeling and observations. J Geophys Res 109(F2):F02,003, DOI 10.1029/2003JF000070
Roos PC, Hulscher SJMH, de Vriend HJ (2008) Modelling the morphodynamic impact of offshore sandpit geometries. Coastal Engineering 55(9):704–715, DOI 10.1016/j.coastaleng.2008.02.019
Sanay R, Voulgaris G, Warner JC (2007) Tidal asymmetry and residual circulation over linear sandbanks and their implication on sediment transport: A process-oriented numerical study. J Geophys Res 112(C12):C12,015, DOI 10.1029/2007JC004101
Sekine M, Parker G (1992) BedLoad Transport on Transverse Slope. I. Journal of Hydraulic Engineering 118(4):513–535, DOI 10.1061/(ASCE)0733-9429(1992)118:4(513)
Smith DB (1988) Stability of an offset kink in the North Hinder Bank. In: De Boer P, Van Gelder A, Nio SD (eds) Tide-Influenced Sedimentary Environments and Facies., D. Reidel Publishing Company, Dordrecht, pp 65–78
Van Lancker VR, Bonne WM, Velegrakis AF, Collins MB (2010) Aggregate extraction from tidal sandbanks: Is dredging with nature an option? Introduction. Journal of Coastal Research pp 53–61
Van Rijn LC (1993) Principles of sediment transport in rivers, estuaries and coastal seas. Aqua publications Amsterdam
Whitehouse RJS, Harris JM, Sutherland J, Rees J (2011) The nature of scour development and scour protection at offshore windfarm foundations. Marine Pollution Bulletin 62(1):73–88, DOI 10.1016/j.marpolbul.2010.09.007
Williams JJ, MacDonald NJ, O'Connor BA, Pan S (2000) Offshore sand bank dynamics. Journal of Marine Systems 24(12):153–173, DOI 10.1016/S0924-7963(99)00085-8
Zimmerman JTF (1982) On the Lorentz linearization of a quadratically damped forced oscillator. Physics Letters A 89(3):123–124, DOI 10.1016/0375-9601(82)90871-4

## Appendix A: Forcing of the basic flow

The basic flow is written as a truncated Fourier series according to

$$(u_0, v_0) = \sum_{p=-2}^{2} (U_{0p}, V_{0p}) \exp(ip\sigma t)\,. \tag{24}$$

The complex Fourier coefficients $(U_{0p}, V_{0p})$ relate to the magnitude $\gamma_0$ and direction $\vartheta_0$ in rads in case of the residual flow ($p = 0$) or semi-major axis $\gamma_p$, ellipticy $\varepsilon_p$, inclination $\vartheta$ in rads and phase $\psi_p$ in rads for an $M_2$- or $M_4$-tide ($p = \pm 1$ and $p = \pm 2$ respectively). The magnitude $\gamma$ has been scaled according to $\gamma = \frac{\gamma^*}{U^*}$, in which $\gamma^*$ is the amplitude of the tidal flow in m/s. We formulate the following relation between flow properties and the Fourier coefficients of the tidal flow according to

$$U_{00} = \gamma_0 \cos \vartheta_0, \qquad V_{00} = \gamma_0 \sin \vartheta_0 \tag{25}$$

for $p = 1$, otherwise:

$$U_{0p} = \frac{1}{2}\gamma_{|p|} (\cos \vartheta_{|p|} + \varepsilon_{|p|} \sin \vartheta_{|p|}) \exp(-\frac{p}{|p|} i\psi_p)\,, \tag{26}$$

$$V_{0p} = \frac{1}{2}\gamma_{|p|} (\sin \vartheta_{|p|} - \varepsilon_{|p|} \cos \vartheta_{|p|}) \exp(-\frac{p}{|p|} i\psi_p)\,. \tag{27}$$

## Appendix B: Basic flow solution

In Eq. (18), $\phi_0$ describes the lowest order flow, which is spatially uniform oscillatory flow over a flat bed $h = h_0$, as triggered by the spatially uniform yet time-dependent tidal forcing terms $(F(t), G(t))$. It relates to the Fourier coefficients of tidal flow over a flat bed (Eqs. 12-13):

$$(u_0, v_0) = \sum_{p=-2}^{2} (U_{0p}, V_{0p}) \exp(ip\sigma t)\,. \tag{28}$$

The spatial uniformity implies that the vorticity vanishes over the domain: $\eta_0 = 0$.

## Appendix C: First order flow solution

$\phi_1$ describes the linear response to bed perturbation $h_1$. To this end, we evaluate Eq. (17) at $\mathscr{O}(\varepsilon)$:

$$\mathscr{L}_0\eta_1 = \underbrace{\left[\frac{f}{h_0}\frac{\partial h_1}{\partial x} - \frac{r}{h_0^2}\frac{\partial h_1}{\partial y}\right]}_{R_1} u_0 + \underbrace{\left[\frac{f}{h_0}\frac{\partial h_1}{\partial y} + \frac{r}{h_0^2}\frac{\partial h_1}{\partial x}\right]}_{S_1} v_0 \tag{29}$$

with linear operator $\mathscr{L}_0 = \partial/\partial t + u_0\partial/\partial x + v_0\partial/\partial y + r/h_0$. It shows that the first order vorticity is advected by the basic flow and forced by the interaction between the first order topography (including bottom friction and Coriolis effects) and basic flow: $R_1 u_0$ and $S_1 v_0$. Note that the terms $R_0 u_1$ and $S_0 v_1$ vanish, because the lowest order topography is spatially uniform. It follows that $\eta_1$ varies both spatially and temporally:

$$\eta_1(x,y,t) = \sum_{m=-M}^{M}\sum_{n=-M}^{M} \hat{\eta}_{1mn}(t)\exp(i[k_m x + l_n y])\,, \tag{30}$$

in which the Fourier coefficients are

$$\hat{\eta}_{1mn}(t) = \sum_{p=-P}^{P} E_{1mnp}\exp(ipt)\,. \tag{31}$$

Herein, $P$ is the temporal truncation number and $E_{1mnp}$ are the spatio-temporal Fourier components. Because the basic flow is spatially uniform, the spatial modes (denoted by subscripts $m$ and $n$) do not interact. Hence, the Fourier components of the vorticity of each spatial mode can be solved separately via a first order linear system:

$$L_{mn}E_{1mn} = b_{1mn}\,. \tag{32}$$

with $(2P+1)\times(2P+1)$ matrix $L_{mn}$, which for $P=2$ is given by

$$\begin{bmatrix}
-2i + A_0 + \frac{r}{h_0} & A_{-1} & A_{-2} & 0 & 0 \\
A_1 & -i + A_0 + \frac{r}{h_0} & A_{-1} & A_{-2} & 0 \\
A_2 & A_1 & A_0 + \frac{r}{h_0} & A_{-1} & A_{-2} \\
0 & A_2 & A_1 & i + A_0 + \frac{r}{h_0} & A_{-1} \\
0 & 0 & A_2 & A_1 & 2i + A_0 + \frac{r}{h_0}
\end{bmatrix}$$

with shorthand notation $A_p = ik_m U_{0p} + il_n V_{0p}$. Furthermore, $E_{1mn}$ is a column vector with elements $E_{1mnp}$ as is forcing term $b_{1mn}$ with elements

$$b_{1mnp} = \left(\left[\frac{fik_m}{h_0} - \frac{ril_n}{h_0^2}\right]U_{0p} + \left[\frac{fil_n}{h_0} + \frac{rik_m}{h_0^2}\right]V_{0p}\right). \tag{33}$$

Next, we combine the continuity equation (8) with the definition of vorticity (Eq. 16) to obtain an expression for the Fourier coefficients of the tidal flow:

$$\hat{u}_{1mn} = \frac{il_n\hat{\eta}_{1mn} + ik_m a\hat{h}_{1mn}/h_0}{k_m^2 + l_n^2}\,, \tag{34}$$

$$\hat{v}_{1mn} = \frac{-ik_m\hat{\eta}_{1mn} + il_n a\hat{h}_{1mn}/h_0}{k_m^2 + l_n^2} \tag{35}$$

with $a = ik_m u_0 + il_n v_0$.

## Appendix D: Higher order flow solutions

$\phi_j$ with $j = 2,3,\ldots,J$ describe subsequent nonlinear contribution terms to the hydrodynamic solution. These contributions are of higher order in $h_1$, i.e. quadratic for $j=2$, cubic for $j=3$ and so on up to order $J$. The forcing terms of the $j$-th order vorticity $\eta_j$ emerge as convolution sums of lower order quantities:

$$\mathscr{L}_0\eta_j = \sum_{j'=1}^{j}\Big(\underbrace{R_{j'}u_{j-j'} + S_{j'}v_{j-j'}}_{\substack{\text{Coriolis and}\\ \text{frictional torques}}} - \underbrace{\left[u_{j'}\frac{\partial\eta_{j-j'}}{\partial x} + v_{j'}\frac{\partial\eta_{j-j'}}{\partial y}\right]}_{\text{advection}} - \underbrace{\mu_{j'}\eta_{j-j'}}_{\substack{\text{depth effect}\\ \text{on friction}}}\Big) \tag{36}$$

Herein, $R_{j'}$, $S_{j'}$ and $\mu_{j'}$ are the $j'$-th order expansions of the functions $R$, $S$ and $\mu$ according to:

$$R_j = (-1)^{j-1}\left(\frac{h_1}{h_0}\right)^{j-1}\left[\frac{f}{h_0}\frac{\partial h_1}{\partial x} - \frac{jr}{h_0^2}\frac{\partial h_1}{\partial y}\right], \tag{37}$$

$$S_j = (-1)^{j-1}\left(\frac{h_1}{h_0}\right)^{j-1}\left[\frac{f}{h_0}\frac{\partial h_1}{\partial y} + \frac{jr}{h_0^2}\frac{\partial h_1}{\partial x}\right], \tag{38}$$

$$\mu_j = (-1)^{j}\left(\frac{h_1}{h_0}\right)^{j}\frac{r}{h_0}\,. \tag{39}$$

Contrary to the first order flow solution, the spatial modes in the nonlinear forcing terms in Eq. (36) do interact. Hence, spatial convolution sums need to be evaluated in all forcing terms. We use the pseudospectral method to compute these. Furthermore, an additional temporal convolution sum needs to be computed in the advective term. With the forcing known, the $j$-th order vorticity $\eta_j$ and flow $(u_j,v_j)$, can be computed in a way similar to the first order hydrodynamic solution, see Eqs. (32) - (35). This results in the Fourier coefficients for the tidal flow (except the spatial uniform part):

$$\hat{u}_{jmn} = \frac{il_n\hat{\eta}_{jmn} + ik_m a/h_0}{k_m^2 + l_n^2}, \tag{40}$$

$$\hat{v}_{jmn} = \frac{-ik_m\hat{\eta}_{jmn} + il_n a/h_0}{k_m^2 + l_n^2} \tag{41}$$

with $a = ik_m\{h_1u_{j-1}\}_{mn} + il_n\{h_1v_{j-1}\}_{mn}$. Here, $\{h_1u_{j-1}\}_{mn}$ and $\{h_1v_{j-1}\}_{mn}$ refer to the contributions of the spatial convolution of the quantities $h_1u_{j-1}$ and $h_1v_{j-1}$ to mode $(m,n)$.

The spatially uniform part of the flow is treated separately. Hereto, we apply the spatially averaged momentum equations to obtain:

$$\begin{bmatrix} ip+\mu_0 & -f \\ f & ip+\mu_0 \end{bmatrix} \begin{bmatrix} U_{j00p} \\ V_{j00p} \end{bmatrix} = \begin{bmatrix} -C_{j00p} \\ -D_{j00p} \end{bmatrix}, \tag{42}$$

in which $C_{j00p}$ and $D_{j00p}$ are the $p$-th order temporal Fourier coefficients according to

$$\hat{c}_{j00} = \sum_{j'=1}^{j} \left\{ \mu_{j'}u_{j-j'} + u_{j'}\frac{\partial u_{j-j'}}{\partial x} + v_{j'}\frac{\partial u_{j-j'}}{\partial y} \right\}_{00}, \tag{43}$$

$$\hat{d}_{j00} = \sum_{j'=1}^{j} \left\{ \mu_{j'}v_{j-j'} + u_{j'}\frac{\partial v_{j-j'}}{\partial x} + v_{j'}\frac{\partial v_{j-j'}}{\partial y} \right\}_{00}. \tag{44}$$

The solution of the linear system in Eq. (42) is given by

$$\hat{u}_{j00} = \frac{(ip+\frac{r}{h})\hat{c}_{j00} + f\hat{d}_{j00}}{(ip+\frac{r}{h})^2 + f^2}, \tag{45}$$

$$\hat{v}_{j00} = \frac{-f\hat{c}_{j00} + (ip+\frac{r}{h})\hat{d}_{j00}}{(ip+\frac{r}{h})^2 + f^2}. \tag{46}$$